

Chirality and Clock transitions in Twisted Dipolar Clusters

Paula Mellado,¹ Xavier Cazor,¹ and Andres Concha^{1,*}

¹*Facultad de Ingeniería y Ciencias, Universidad Adolfo Ibáñez.
Diagonal las Torres 2640, Santiago, Chile.*

(Dated: February 2, 2026)

We study samples and a dipolar model of magnetic rods arranged on twisted polygonal clusters in terms of the twist angle. We find that the relative twist between polygons induces noncollinear chiral phases, ranging from flux vortex closure to hedgehog like radial configurations. Chirality, quantified in terms of a bond order parameter, is an emergent property that behaves here as an Ising variable. The chiral configurations of the systems can be understood in terms of chirality and clock index order parameters, whose evolution with twist occurs through two types of first order phase transitions. Within a fixed Ising chiral sector, the clock index, rooted in the C_N invariance of the polygons, characterizes chiral textures that share chirality. As the twist increases, it continuously shifts the preferred relative clock phase, but the N -fold anisotropy only allows discrete orientations; the competition produces a tilted N -fold energy landscape whose global minimum hops discontinuously between clock sectors. As the number of sites in the polygon grows, the resulting response displays a nonlinear crossover from rigid, Ising-like behavior to an almost $U(1)$ -invariant regime, governed by a twist-induced suppression of the emergent Z_N clock anisotropy. A Landau phenomenology captures these trends and naturally extends to bilayer lattices, where we show that twisted honeycomb systems realize an effective sine-Gordon theory with twist-controlled transitions between isolated domain walls and domain-wall lattices.

I. INTRODUCTION

Chiral magnetic structures [1, 2] arise from broken inversion symmetry in the crystal unit cell [3, 4]. Magnetochiral textures are usually governed by antisymmetric, spin-orbit-driven interactions such as the Dzyaloshinskii-Moriya interaction (DMI) [1–3, 5–10]. Yet DMI is not the only mechanism that stabilizes chiral textures; long-range dipolar interactions can also generate and stabilize chiral order in thin films and low-dimensional lattices [11–19]. Magnetochirality has traditionally been engineered through the intrinsic crystal and electronic structure by material and composition choice [20]. More recently, it has been shown that a small relative twist between bilayers with antiferromagnetic and ferromagnetic coupling can induce noncollinear spin configurations [21], even without intrinsic chiral interactions [22, 23]. In lattices with discrete rotational symmetry, chirality is described by a clock-like angle [24], whose energy minima correspond to the symmetry-allowed orientations of flux-closure textures [25]. Dipolar interactions favor such chiral states stabilizing vortical or radial configurations with finite vector chirality. Magnetochiral order then amounts to selecting one clock state, while fluctuations and defects appear as domain walls between distinct chiral sectors. Discrete-symmetry clock models [26–28] provide a minimal description of systems whose orientational order is restricted to a finite set of angles, interpolating between Ising-like and continuous $U(1)$ behavior as the number of states increases [24]. They describe magnetic systems where lattice symmetry or anisotropic interactions pin the order parameter to discrete directions, producing domain walls, topological defects, and clock-anisotropy crossovers [29, 30].

In the continuum limit, the Z_N clock model maps

to a sine-Gordon field theory [30, 31], where discrete anisotropy appears as a periodic locking potential for an angular order parameter [32]. Low-energy excitations are domain walls between neighboring clock states, with tension set by the clock pinning strength. In bilayers, twisting tunes this pinning: relative rotation frustrates the discrete anisotropy, softening the sine-Gordon potential and promoting domain-wall proliferation [33, 34]. Twisted bilayers thus interpolate between regimes with isolated domain walls and dense domain-wall lattices, indicating an emergent restoration of $U(1)$ symmetry at large twist or weak pinning.

Summary of Results Aimed at understanding the role of geometrical twist in the fate of chiral magnetic phases in heterostructures, we study the ground states of a set of magnets located at the sites of a couple of polygons that are mutually rotated with respect to their centroid. Experiments with magnetic rods at twisted hexagons and simulations of point dipoles at several N -gons show relaxation into noncollinear textures with finite intrinsic chirality. Depending on polygon geometry and twist, the systems host ordered chiral phases with circulating or inward-outward spin patterns. This chiral order arises from a twist-induced nonreciprocal interpolygon torque generated by the nonlocal magnetic field of the rotated layers. Acting as an effective chiral field, this torque reshapes the minimizing spin texture and produces sharp chirality switching with twist angle. A Landau phenomenology captures these effects and extends to twisted honeycomb bilayers, whose low-energy theory maps onto a sine-Gordon model with twist-controlled domain-wall phases.

The paper is organized as follows. Section II introduces the system, describes the geometry of twisted polygonal bilayers, and presents equilibrium states for hexago-

nal twisted arrays versus twist. Section III analyzes the emergence of chirality in twisted clusters as a function of twist angle, presents energy-minimization results for point-dipole equilibrium states, and studies chirality order parameters and clock index versus twist angle for several types of polygonal clusters. Section IV addresses the Landau free energy, and Section V the effective hamiltonian. Section VI extends the analysis to twisted hexagonal bilayers. Section VII summarizes our findings.

II. MAGNETIC CHIRAL TEXTURES IN TWISTED BI-HEXAGONS

We consider two identical polygons, each consisting of N easy-plane magnetic rods arranged at the vertices of a regular N -gon, as shown in the samples of Fig.1. The dipole moments are $\mathbf{m}_i = m_0(\cos \theta_i, \sin \theta_i, 0)$, so the equilibrium configuration is fully specified by the set of angles $\{\theta_i\}$. The two polygons are separated along the z direction. The upper polygon is rotated by a twist angle ϕ with respect to the lower one around the z axis, as shown in Fig. 1. The position of the i -th dipole is written as

$$\mathbf{r}_i(\phi) = \begin{cases} \mathbf{R}_i, & i = 1, \dots, N, \\ \mathcal{R}_z(\phi) \mathbf{R}_{i-N} + d\hat{\mathbf{z}}, & i = N+1, \dots, 2N, \end{cases} \quad (1)$$

where $\mathbf{R}_i = R_N(\cos \frac{2\pi i}{N}, \sin \frac{2\pi i}{N}, 0)$ denotes the in-plane coordinates of a regular N -gon of unit radius, R_N is the distance from the center of a dipole to the centroid of the polygon, d is the distance between layers, and $\mathcal{R}_z(\phi)$ is a rotation matrix about the z axis. The distance between nearest neighbor dipoles is a . Fig. 2 shows the relaxed system for twelve twist angles $\phi \in (0, \frac{2\pi}{6})$. At low twist ($\phi \approx 0$), magnets form a closed flux (See Fig. 2) in a head-to-tail arrangement. The magnetic rods in different layers arrange antiferromagnetically. This configuration minimizes the total dipolar energy. As ϕ grows, the x-y symmetry breaks, and the twisted magnets rearrange in the x-y plane to preserve flux closure (Fig.2(b-d)). For $\phi \approx 30^\circ$ (Fig.2(e,f)), the top and bottom hexagonal sites are equidistant, and the magnets lie on a circle of radius R_0 , with nearest neighbors belonging to different layers. For larger ϕ , the process reverses (Fig.2(g-l)). However, due to the lack of symmetry for internal fields, the system exhibits hysteresis[35]. Thus, configurations for ϕ increasing from $\pi/6$ to $\pi/3$ differ from those in the first half of the twist (Fig.2(a-f)). All observed textures are chiral, but some states feature mostly antiparallel nearest neighbors, as in Figs.2(i,j).

III. TWISTED POLYGONS

We model the magnets as point dipoles, so the total magnetostatic energy is written as the sum of intralayer

and interlayer contributions: contributions

$$H_{\text{dip}}^{\text{bil}} = H_{bb} + H_{tt} + H_{bt}(\phi), \quad (2)$$

with

$$H_{\ell\ell} = \sum_{i < j \in \ell}^N \left[\frac{\mathbf{m}_{i\ell} \cdot \mathbf{m}_{j\ell}}{r_{ij,\ell\ell}^3} - 3 \frac{(\mathbf{m}_{i\ell} \cdot \mathbf{r}_{ij,\ell\ell})(\mathbf{m}_{j\ell} \cdot \mathbf{r}_{ij,\ell\ell})}{r_{ij,\ell\ell}^5} \right], \quad (3)$$

$$\ell \in \{b, t\},$$

$$H_{bt}(\phi) = \sum_{i \in b}^N \sum_{j \in t}^N \left[\frac{\mathbf{m}_{ib} \cdot \mathbf{m}_{jt}}{r_{ij,bt}^3} - 3 \frac{(\mathbf{m}_{ib} \cdot \mathbf{r}_{ij,bt})(\mathbf{m}_{jt} \cdot \mathbf{r}_{ij,bt})}{r_{ij,bt}^5} \right], \quad (4)$$

$\{b, t\}$ label bottom and top polygons, $\mathbf{r}_{ij} = \mathbf{r}_i(\phi) - \mathbf{r}_j(\phi)$ and m_0 is the intensity of the magnetic moment. Hereafter, we use $m_0 = 1$, $a = 1$, and $d = 0.5$. The energy scale is the dipolar energy between nearest neighbor dipoles, $E_0 = \frac{\mu_0 m_0^2}{4\pi a^3}$.

For an angle ϕ , the equilibrium magnetic texture is found by minimizing Eq. (2) with respect to all angles $\{\theta_i\}$. Figs. 3(a–e) show the equilibrium states for five polygonal families ($N = 3, 4, 5, 6, 8$). At $\phi = 0$, all clusters form an antiferromagnetic vortex state where the top and bottom dipoles create a flux-closure texture. Neighboring polygons have opposite vortex handedness, canceling magnetic torques (ferrochiral state). As ϕ increases, the in-plane components of the internal field acquire a term proportional to ϕ , generating a torque along $\pm z$. This twist-induced torque rotates the magnets, producing ferrochiral textures consistent with experiments (Figs. 2(b–l)).

A. Ferrochiral Bistability

The z-component of the bond chirality [36] is,

$$\kappa = \sum_{i=1}^N \hat{\mathbf{z}} \cdot (\mathbf{m}_i \times \mathbf{m}_{i+1}) = \sum_{i=1}^N \sin(\theta_{i+1} - \theta_i), \quad \theta_{N+1} \equiv \theta_1. \quad (5)$$

For a single regular polygon, the maximal value of κ occurs when $\theta_{i+1} - \theta_i = \Delta\theta = \frac{2\pi}{N}$, $\kappa_{\text{max}}(N) = \sum_{i=1}^N \sin(\frac{2\pi}{N}) = N \sin(\frac{2\pi}{N})$. We computed chirality separately for the lower and upper polygons, κ_b , κ_t , and defined the quantity

$$\chi = \frac{1}{2|\kappa_{\text{max}}|} (\kappa_b + \kappa_t) \quad (6)$$

with $\kappa_\ell = \sum_{i=1}^N \sin(\theta_{i+1}^{(\ell)} - \theta_i^{(\ell)})$. In the ferrochiral state $\kappa_b = \kappa_t$. Equation 5 gives $\kappa_\ell = +|\kappa_{\text{max}}|$ since chirality is defined identically for the top and bottom polygons, and κ is even under time reversal. $\chi = +1 \equiv \chi_0$ corresponds to the vortex (V) states (Figs.2(a-h), Figs.2(k,l), and top row of 3). In the radial chiral state (R), $\kappa < 0$. If N is even, $\kappa = -|\kappa_{\text{max}}|$ and $\chi = -\chi_0$; if N is odd,

$-\lvert\kappa_{\max}\rvert < \kappa < 0$ and $-\chi_0 < \chi < 0$ (Figs.2(i,j) and 3 middle row). V has nearly uniform angle differences $\sim \pm 2\pi/N$, which favor dipolar interactions. A R (hedgehog–antihog) state, instead, has nonuniform angle differences with opposite contributions to $\sin(\theta_{i+1} - \theta_i)$, increasing dipolar energy and causing frustration.

We computed $\chi(\phi)$ in twisted triangular, square, pentagonal, hexagonal, and octagonal bilayers for $\phi \in (0, 2\pi/N)$. In all cases, the system formed a ferrochiral state [37, 38] for all ϕ . For $N = 3, 4, 5, 6$ (Figs.4(a–d)), chirality depends strongly on ϕ and remains finite for all twist angles, displaying stepwise jumps as the system switches between topologically distinct textures. Because these bipolygonal structures only access V and R states, these configurations form two chiral Ising sectors that are topologically distinct and not connected by a smooth spin rotation. For $N \geq 8$, Fig.4(e), χ is independent of ϕ .

Chirality curves for triangles, squares, pentagons, and hexagons collapse onto a common form (Fig.4(a–d)), showing that the leading twist response is set by the C_N clock anisotropy [30]. Deviations from this collapse quantify higher-harmonic contributions, which rapidly diminish with increasing N . This behavior demonstrates that the evolution from rigid, Ising-like chirality in the triangle, through multi-plateau clock behavior in the hexagon [39], to an almost $U(1)$ -invariant response in the octagon is governed by a clock-anisotropy crossover induced by the discrete lattice symmetry under twisting.

IV. LANDAU FREE ENERGY

At $\phi = 0$, the interlayer field \mathbf{B} is locally collinear with the dipoles and exerts no torque. For finite ϕ , the twist generates a transverse component of the field proportional to ϕ , producing a net torque along \hat{z} . Considering the free-energy density $F(\mathbf{r})$ of one layer subject to the weak, slowly varying twist-induced magnetic field $\delta\mathbf{B}_{\text{twist}}$. In the linear response regime, a gradient expansion of the free-energy density $F(\mathbf{r})$ of one layer subject to the weak, slowly varying twist-induced magnetic field yields the field conjugate to chirality [12]

$$h_{\kappa, N} = (\nabla \times \delta\mathbf{B}_{\text{twist}})_z \simeq \phi (\partial_y B_{\phi=0} - \partial_x B_{\phi=0}), \quad (7)$$

For a given twist, the form of $h_{\kappa, N}$ is fixed by N . Without $h_{\kappa, N}$, the system is in one of two V configurations with $\chi = +1$: clockwise (CW) or counterclockwise (CCW). When $\phi \neq 0$ the R texture creates a new local minimum in the energy, separated from the global minimum by a barrier that decreases with ϕ . At a critical twist $\phi = \phi^{c1}$, V and R states are equally favorable, and at $\phi > \phi^{c1}$ the system switches to R. A minimal Landau functional for the ferrochiral state $\kappa_t = \kappa_b = \kappa$ is $F_{\kappa}(\kappa, \phi) = \frac{\tau}{2}\kappa^2 + \frac{u}{4}\kappa^4 + \frac{w}{6}\kappa^6 - h_{\kappa, N}(\phi)\kappa$, with $u < 0$, $w > 0$. At zero twist, the energy has a single minimum corresponding to V. As $|\phi|$ increases, $h_{\kappa, N}(\phi)$ tilts the potential and gradually stabilizes a second local minimum corresponding to R.

This minimum is separated by an energy barrier whose height decreases continuously with increasing $|\phi|$. The critical twist ϕ^{c1} can be estimated by using

$$\Delta F(\phi) \equiv F_{\chi}(+\chi_0; \phi) - F_{\chi}(-\chi_0; \phi) \simeq -2h_{\chi, N}(\phi)\chi_0.$$

The transition occurs when $h_{\chi, N}(\phi^{c1}) \simeq 0$. For the minimal symmetry-allowed form $h_{\chi, N}(\phi) = \lambda_{\chi} \sin(N\phi)$, this yields

$$\phi^{c1} \simeq \frac{\pi}{N}, \quad (8)$$

The triangular cluster supports only single radial and single vortex chiral phases, Fig.4(a). In contrast, the hexagonal twisted system shows multiple plateaus in χ , indicating distinct clock-like chiral textures within the same Ising sector, Fig.4(d). This suggests lattice-harmonic effects beyond the rigid chiral regime of the triangle. Although the dipolar Hamiltonian is globally spin-rotation invariant, this symmetry is reduced once dipoles occupy fixed positions $\{\mathbf{r}_i\}$.

We consider low-energy chiral textures described by angles $\{\theta_i\}$ and a collective rotation $\theta_i \rightarrow \theta_i + \alpha$, which defines a phase α . Substituting it into the dipolar Hamiltonian gives a periodic energy $E(\alpha)$. Because the dipoles form a regular N -gon, the system is invariant only under C_N rotations, $E(\alpha) = E(\alpha + \frac{2\pi m}{N})$, $m \in \mathbb{Z}$. The Fourier series of $E(\alpha)$ contains only C_N -compatible harmonics, $E(\alpha) = E_0 - \sum_{p=1}^{\infty} V_{pN} \cos(pN\alpha - \theta_{pN})$. The leading term is the N -fold harmonic, $E(\alpha) \simeq E_0 - V_N \cos(N\alpha - \theta_0)$, yielding an emergent Z_N clock anisotropy [40]. The collective phase α is fixed by the internal angular correlations of the texture, where the clock-harmonic amplitude is set by the strength of correlations around the polygon. To leading order, $V_N \propto |\kappa|^N$, since the N -fold harmonic comes from correlated angular differences accumulated around the loop. Thus, clock anisotropy is strong in vortex-like textures and is strongly suppressed in radial configurations. We identify the collective clock phase as $\vartheta \equiv \alpha$. Let $\mathbf{r}_{i\ell}(\phi)$ be the fixed position of site i in layer $\ell \in \{b, t\}$, with \mathbf{r}_{ib} being independent of ϕ , and $\mathbf{r}_{it}(\phi)$ obtained by rigidly rotating the top polygon. Each polygon has a collective clock phase ϑ_{ℓ} associated with a collective rotation of the low-energy texture. Because each polygon has only C_N symmetry, the intralayer energies generate the emergent clock pinning

$$F_{\text{clock}} = - \sum_{\ell \in \{t, b\}} V_N^{(\ell)} |\kappa|^N \cos(N\vartheta_{\ell} - \theta_{0\ell}) \quad (9)$$

where V_N quantifies the breaking of the $U(1)$ rotational symmetry down to C_N . We define the Z_N -projected collective phase of polygon ℓ from the minimized microscopic angles $\{\theta_{i\ell}\}_{i=1}^N$. A convenient definition is obtained from the N -fold harmonic

$$Q_{N,\ell} \equiv \frac{1}{N} \sum_{i=1}^N e^{iN\theta_{i\ell}}, \quad \vartheta_{\ell} \equiv \frac{1}{N} \arg(Q_{N,\ell}), \quad (10)$$

where ϑ_ℓ is defined modulo $2\pi/N$.

The discrete clock index is obtained by binning $\vartheta_\ell(\phi)$ to the nearest Z_N sector,

$$m_\ell(\phi) = \text{Mod}\left(\text{Round}\left[\frac{N}{2\pi}(\vartheta_\ell(\phi) - \vartheta_{0,\ell})\right], N\right), \quad (11)$$

where $\vartheta_{0,\ell}$ is a fixed gauge setting $m_\ell = 0$ for a chosen configuration at a selected twist. Equivalently, the inverse relation expresses the pinned clock phase in terms of m_ℓ as

$$\vartheta_\ell(\phi) \approx \vartheta_{0,\ell} + \frac{2\pi}{N} m_\ell(\phi), \quad m_\ell \in \{0, 1, \dots, N-1\}, \quad (12)$$

Fig.5(a-e) shows $m(\phi)$ for $N = 3, 4, 5, 6, 8$ respectively. The plateaus of $m_\ell(\phi)$ and their jumps by ± 1 reflect discrete jumps between neighboring minima of the effective Z_N clock potential with ϕ . Between different clock textures, only the clock angle changes as they share the same χ , differing only by a global rotation, separated by clock-pinning barriers. The C_N pinning comes from the N angular Fourier harmonic of the microscopic interaction energy, which is exponentially small in N , $V_N \sim e^{-N/\xi_\theta}$, where ξ_θ is an angular smoothness scale set by the interaction range and inter-polygon separation. As N increases at fixed nearest-neighbor spacing, the leading symmetry-allowed harmonic moves to higher order and is strongly suppressed. At fixed spacing, increasing N increases the polygon radius $R_N \sim Na/(2\pi)$, making the object approach a smooth ring. For the octagonal geometry, this drives the effective chiral field to zero and a flat chiral response (Fig. 4(e)).

Examining Fig.5(d) and Fig.4(d), we find that clock-phase switching is strongly enhanced in the R sector. This asymmetry stems from the different dipolar frustra-

tion patterns of the two chiral textures. In the R sector, the pronounced enhancement of clock-phase switching results from a strong suppression of the emergent Z_N clock-pinning amplitude, set by the coherence of angular correlations around the polygon. In V textures, circulating spins add constructively to the N -fold harmonic, producing strong clock pinning and large energy barriers between clock sectors. In R textures, alternating angular differences cause destructive interference of the N -fold harmonic, strongly suppressing $V_N(\kappa)$. Consequently, the R sector has lower barriers and frequent clock-phase switching under twist.

The interpolygon dipolar coupling, determined by the dipolar scale, interlayer separation, and in-plane lattice constant, is accounted for by

$$F_{\text{inter}} = -J_\perp(\phi) |\kappa|^2 \cos(\vartheta_t - \vartheta_b - \delta_0(\phi)). \quad (13)$$

$J_\perp(\phi)$ is the effective interlayer phase stiffness, and $\delta_0(\phi)$ is a geometric phase bias encoding the relative registry of the two polygons. For an N -gon, the clock phase ϑ has a period $2\pi/N$, so a uniform rotation by ϕ shifts the preferred interlayer phase difference by $N\phi$, $\delta_0(\phi) = \delta^* + N\phi$, where δ^* is a constant set by the untwisted stacking and the reference phases of $\vartheta_{t,b}$. $\delta_0(\phi)$ provides the leading twist dependence relevant for the clock-phase transitions. Overall, the slow collective modes of twisted polygonal clusters are described by the clock angle ϑ and the chirality κ . In the continuum-ring limit, the interlayer coupling depends on the relative twist ϕ , $\vartheta_t - \vartheta_b - \phi$, so ϕ can be absorbed by a phase shift. For polygons, this U(1) symmetry is reduced to C_N by the leading lattice harmonic (clock anisotropy), which pins ϑ to one of N discrete minima and breaks the gauge freedom, allowing for the chiral-field term $h_N(\phi) = \sum_m \lambda_{m,N} \sin(mN\phi)$. Thus, a nonzero twist generates a conjugate geometric drive that tilts the clock landscape,

$$F_{\text{drive}}(\vartheta; \phi) = -h_N(\phi) \cos(\vartheta - \vartheta_0), \quad h_N(\phi) \simeq \lambda_{1,N} \sin(N\phi), \quad (14)$$

up to an unimportant phase offset ϑ_0 . Increasing N simultaneously (i) shifts the response to the higher harmonic $N\phi$ and (ii) suppresses its amplitude, since both V_N and $\lambda_{1,N}$ rapidly decrease as the polygon approaches a ring. This accounts for the progression in Fig.5: for the triangle, the effective anisotropy is strong, and the dynamics reduce to Ising-like switching between two chiral sectors; for the hexagon, the clock term creates multiple

metastable minima, and the chirality shows six plateaus corresponding to distinct clock-locked textures; for the octagon, the clock anisotropy and the leading harmonic of the twist-induced chiral drive are so weak that $\kappa(\phi)$ is flat.

Collecting the lowest-order symmetry-allowed contributions, the coupled chiral-clock free energy for twisted polygons takes the form

$$F(\kappa, \vartheta_t, \vartheta_b; \phi) = \frac{r}{2} \kappa^2 + \frac{u}{4} \kappa^4 + \frac{w}{6} \kappa^6 - 2h_{\kappa,N}(\phi) \kappa - V_N(\kappa) |\kappa|^N (\cos(N\vartheta_b - \theta_{0b}) - \cos(N\vartheta_t - \theta_{0t})) - J_\perp(\phi) |\kappa|^2 \cos(\vartheta_t - \vartheta_b - \delta^* - N\phi), \quad (15)$$

($u|0, w|0$). Eq.15 gives a hierarchy of phase transitions set by the larger chiral barrier $\sim w\kappa^N$ and the smaller clock barrier $\sim V_N\kappa^N$: (i) a first-order chiral transition in κ , controlled by κ and $h_{\kappa,N}(\phi)$, where the twist-induced internal torque causes a first-order Ising jump in κ with hysteresis, and $2h_{\kappa,N}(\phi)$ tilts the κ double well; (ii) within a fixed chiral sector, a sequence of twist-driven first-order clock transitions of ϑ , governed by the discrete Z_N pinning and the mismatch $\delta_0(\phi)$.

V. EFFECTIVE HAMILTONIAN

In a given chiral sector, the chirality amplitude is fixed, we set

$$\kappa \rightarrow \kappa_\chi \quad (\chi \text{ fixed}), \quad (16)$$

and define

$$V_N^{(\chi)} \equiv V_N(\kappa_\chi) |\kappa_\chi|^N, \quad K_\perp^{(\chi)}(\phi) \equiv J_\perp(\phi) |\kappa_\chi|^2. \quad (17)$$

Dropping constant factors of κ , the only remaining slow variables are the clock phases. The interlayer coupling fixes the relative phase, and when it is appreciable, the last term in the free energy locks the relative angle and can be dropped $\vartheta_t - \vartheta_b \equiv \vartheta_- \sim \delta_0(\phi) \pmod{2\pi}$, which allows using a single clock variable

$$\vartheta \equiv \vartheta_b, \quad \vartheta_t = \vartheta + \delta_0(\phi).$$

which yields the effective angular Hamiltonian in the chiral sector χ .

$$H^{(\chi)}(\vartheta; \phi) = -V_N^{(\chi)} \cos(N\vartheta - \theta_{0b}) - V_N^{(\chi)} \cos(N\vartheta + N\delta_0(\phi) - \theta_{0t}) \quad (18)$$

We define $A \equiv N\vartheta - \theta_{0b}$, and $B(\phi) \equiv N\delta_0(\phi) - (\theta_{0t} - \theta_{0b})$. In (18), this yields

$$H^{(\chi)}(\vartheta; \phi) = -V_{\text{eff}}^{(\chi)}(\phi) \cos(N\vartheta - \theta_{\text{eff}}(\phi)) \quad (19)$$

with

$$V_{\text{eff}}^{(\chi)}(\phi) \equiv 2V_N^{(\chi)} \left| \cos\left(\frac{B(\phi)}{2}\right) \right|, \quad (20)$$

$$\theta_{\text{eff}}(\phi) \equiv \theta_{0b} - \frac{B(\phi)}{2} \pmod{2\pi}, \quad (21)$$

$$B(\phi) = N\delta^* + N^2\phi - (\theta_{0t} - \theta_{0b}), \quad (22)$$

$$\theta_{\text{eff}}(\phi) = \theta_{\text{eff}}(0) - \frac{N^2}{2}\phi \pmod{2\pi}.$$

In a fixed chiral sector, strong interlayer dipolar locking removes the relative clock phase, leaving a single Z_N clock variable ϑ with twist-induced phase drift $\theta_{\text{eff}}(\phi)$ and a chirality-dependent pinning scale $V_{\text{eff}}^{(\chi)}(\phi)$.

For fixed N , the polygon geometry yields the lowest symmetry-allowed anisotropy term $\cos(N\vartheta)$ in the effective free energy. The amplitude $V_N^{(\chi)}$ follows from the microscopic dipolar Hamiltonian after minimizing over the angles $\{\theta_i\}$ in each polygon. The twist alters the relative in-plane dipole alignment between polygons, thereby shifting the preferred phase and renormalizing the pinning scale (20).

Plateaus are intervals where the minimizer $\vartheta(\phi)$ stays within a $2\pi/N$ sector; switching occurs when $\vartheta(\phi)$ crosses a sector boundary. The effective Hamiltonian (19) has minima

$$\vartheta_k(\phi) = \frac{\theta_{\text{eff}}(\phi) + 2\pi k}{N}, \quad k \in \mathbb{Z}. \quad (23)$$

As ϕ increases, each minimum branch of $\theta_{\text{eff}}(\phi)$ drifts approximately linearly. The observed integer plateaus arise because the index $m(\phi)$ is a sector label that remains constant until $\vartheta_k(\phi)$ crosses a sector boundary at

$$\vartheta = \vartheta_0 + \left(m + \frac{1}{2} \right) \frac{2\pi}{N}, \quad m \in \mathbb{Z}. \quad (24)$$

A switch $m \rightarrow m \pm 1$ occurs when the minimizing branch satisfies

$$\vartheta_k(\phi_c) = \vartheta_0 + \left(m + \frac{1}{2} \right) \frac{2\pi}{N}. \quad (25)$$

Using (23),

$$\theta_{\text{eff}}(\phi_c) = N\vartheta_0 + \left(m + \frac{1}{2} \right) 2\pi - 2\pi k. \quad (26)$$

If $\theta_{\text{eff}}(\phi)$ is monotonic and dominated by the linear drift, then the critical twists

$$\phi_c(m; k) = \frac{2}{N^2} \left[\theta_{\text{eff}}(0) - N\vartheta_0 - \left(m + \frac{1}{2} \right) 2\pi + 2\pi k \right] \quad (27)$$

This predicts an equally spaced plateau structure with spacing

$$\Delta\phi = \phi_c(m+1; k) - \phi_c(m; k) = \frac{4\pi}{N^2}. \quad (28)$$

VI. CONTINUUM MODEL OF TWISTED BILAYER HONEYCOMB LATTICES

Consider a bilayer honeycomb system where each hexagonal cell carries a Z_6 clock phase. Twisting the bilayer introduces a spatially varying phase mismatch in the interlayer coupling. We define the coarse-grained clock-phase fields $\vartheta_\ell(\mathbf{r}) = \frac{1}{6} \arg \left(\frac{1}{6} \sum_{j \in \text{hex}(\mathbf{r}, \ell)} e^{i6\theta_j} \right)$, at the plaquette centers \mathbf{r} . At long wavelengths, the minimal symmetry-allowed continuum functional is

$$\mathcal{F} = \int d^2r \left\{ \frac{\rho_b}{2} |\nabla \vartheta_b|^2 + \frac{\rho_t}{2} |\nabla \vartheta_t|^2 - g_b \cos(N\vartheta_b - \theta_{0b}) - g_t \cos(N\vartheta_t - \theta_{0t}) - K_\perp(\phi) \cos(\vartheta_t - \vartheta_b - \delta_0(\mathbf{r}; \phi)) \right\} \quad (29)$$

$\rho_{b,t}$ are the intralayer phase stiffnesses, $g_{b,t}$ are the local Z_N anisotropies from single-hexagon dipolar physics, and $K_\perp(\phi)$ is the chirality-selective Josephson stiffness [41] that locks the relative orientation of polygonal textures between layers. In twisted bilayers, the phase mismatch becomes spatially varying, $\delta_0(\mathbf{r}; \phi) = \delta^* + \mathbf{G}$ with $\mathbf{G} \sim 6\mathbf{q}_m(\phi) \cdot \mathbf{r}$ and \mathbf{q}_m the moiré lattice wavevector. In a lattice, δ_0 becomes slowly varying since $|\mathbf{G}(\phi)| \propto \phi$. We

define

$$\vartheta_+(\mathbf{r}) = \frac{\vartheta_t + \vartheta_b}{2}, \quad \vartheta_-(\mathbf{r}) = \vartheta_t - \vartheta_b.$$

For large K_\perp , $\vartheta_-(\mathbf{r})$ is large and locks to $\vartheta_-(\mathbf{r}) \sim \delta_0(\mathbf{r}; \phi)$ canceling the last term in Eq.29. Substituting $\vartheta_t = \vartheta_+ + \delta_0/2$, $\vartheta_b = \vartheta_+ - \delta_0/2$ gives an effective single-field functional

$$\mathcal{F}_{\text{SG}}[\vartheta_+] = \int d^2r \left[\frac{\rho_{\text{eff}}}{2} |\nabla \vartheta_+|^2 - g_{\text{eff}}(\mathbf{r}; \phi) \cos(N\vartheta_+ - \Theta_{\text{eff}}(\mathbf{r}; \phi)) \right], \quad (30)$$

with an effective stiffness $\rho_{\text{eff}} \simeq (\rho_b + \rho_t)/2$ and moiré-modulated respective amplitudes and phases

$$g_{\text{eff}}(\mathbf{r}; \phi) \propto \left| \cos\left(\frac{N}{2}\delta_0(\mathbf{r}; \phi) - \frac{\theta_{0t} - \theta_{0b}}{2}\right) \right|, \quad (31)$$

$$\Theta_{\text{eff}}(\mathbf{r}; \phi) = \theta_{0b} - \frac{N}{2}\delta_0(\mathbf{r}; \phi) + \frac{\theta_{0t} - \theta_{0b}}{2}. \quad (32)$$

Equation (30) is the continuum Z_N clock sine-Gordon theory [42–45]. For uniform $\delta_0(\phi)$ (single-cluster twist), Θ_{eff} drifts uniformly, causing global clock-phase drift and discrete sector switching in $m(\phi)$. For spatially varying $\delta_0(\mathbf{r}; \phi)$ (bilayer moiré), $\Theta_{\text{eff}}(\mathbf{r}; \phi)$ becomes a slowly varying substrate phase that generates solitons or domain walls and commensurate–incommensurate physics [46, 47] of Frenkel–Kontorova type [48, 49] in the clock field $\vartheta_+(\mathbf{r})$. At small twist (strong pinning), Eq.32 yields a commensurate regime where ϑ_- is locked near $\vartheta_- \sim \frac{\theta_0}{6} + \frac{\pi}{3}m(r)$, so $m(r)$ forms domains. Domain walls (DWs) are lines with energy cost $\sim \sqrt{\rho g}$. While for single clusters ϕ^{c1} marks the chiral first-order jumps, in a twisted bilayer, there are specific positions \mathbf{r}^c where

the local driving phase meets the switching condition $\delta_0(\mathbf{r}^c; \phi^c) \sim \frac{\pi}{3}(m + \frac{1}{2})$; DWs appear along these lines. At larger twists, $\delta_0(\mathbf{r}; \phi)$ winds in space, so the bilayer cannot remain in a single clock sector. To accommodate the misfit, the system forms a network of phase slips where ϑ_- jumps by $\pi/3$, producing an incommensurate soliton network that, for a honeycomb geometry, typically becomes a triangular or hexagonal moiré DW lattice [50–54].

VII. CONCLUSIONS

With the purpose of studying the effect of geometrical twist on the fate of chiral textures in magnetic systems, we studied isolated clusters composed of a couple of twisted polygons with magnets at their sites. Chirality, quantified in terms of a bond order parameter, is an emergent property that behaves here as an Ising variable. The chiral configurations of the systems can be understood in terms of two order parameters, whose evolution with twist occurs through two types of first or-

der phase transitions. Within a fixed Ising chiral sector, the clock index characterizes chiral textures that share the same sign of chirality. While twist couples to the total chirality acting as a conjugate field that drives a first-order chiral transition, the clock phase undergoes additional first-order transitions due to the competition between N-fold pinning and a twist-dependent interlayer phase mismatch. As the twist increases, it continuously shifts the preferred relative clock phase, but the N-fold anisotropy only allows discrete orientations; the competition produces a tilted N-fold energy landscape whose global minimum hops discontinuously between clock sectors. As N increases, the leading symmetry allowed harmonics of the clock potential move to higher orders. A Landau functional captured the two distinct first-order mechanisms and served as the starting point for deriving, in a given chiral sector, the effective Hamiltonian of the system. In this case, strong interlayer dipolar locking eliminates the relative clock phase, reducing the clock

variables of the two polygons to a single Z_N clock variable. These results allowed us to extend the model to a twisted honeycomb bilayer, where the low energy theory maps onto a sine-Gordon model with twist controlled domain-wall phases.

ACKNOWLEDGMENTS

P.M. and X.C. acknowledge support from the Fondo Nacional de Desarrollo Científico y Tecnológico (Fondecyt) under Grant No. 1250122. A.C. was partially supported by FONDECYT Regular No. 1250681.

DATA AVAILABILITY STATEMENT

The data that support the findings of this study are available from the corresponding author upon reasonable request.

* paula.mellado@uai.cl

- [1] N. Nagaosa and Y. Tokura, “Topological properties and dynamics of magnetic skyrmions,” *Nature nanotechnology* **8**, 899–911 (2013).
- [2] M. Mohylna, F. G. Albarracín, M. Žukovič, and H. Rosales, “Spontaneous antiferromagnetic skyrmion/antiskyrmion lattice and spiral spin-liquid states in the frustrated triangular lattice,” *Physical Review B* **106**, 224406 (2022).
- [3] L. Camosi, N. Rougemaille, O. Fruchart, J. Vogel, and S. Rohart, “Micromagnetics of antiskyrmions in ultrathin films,” *Physical Review B* **97**, 134404 (2018).
- [4] Y. Pomeau, “Three short stories on chiral structures in condensed matter,” in *Growth and Form: Nonlinear Aspects* (Springer, 1991) pp. 415–429.
- [5] A. Casher and L. Susskind, “Chiral magnetism (or magnetohydrochirronics),” *Physical Review D* **9**, 436 (1974).
- [6] S. Tomita, H. Kurosawa, T. Ueda, and K. Sawada, “Metamaterials with magnetism and chirality,” *Journal of Physics D: Applied Physics* **51**, 083001 (2018).
- [7] A. Thiaville and A. Fert, “Twisted spin configurations in thin magnetic layers with interface anisotropy,” *Journal of magnetism and magnetic materials* **113**, 161–172 (1992).
- [8] I. E. Dzyaloshinskii, “On the magneto-electrical effects in antiferromagnets,” *Soviet Physics JETP* **10**, 628–629 (1960).
- [9] I. Dzyaloshinskii, “A thermodynamic theory of weak ferromagnetism of antiferromagnetics,” *J. Phys. Chem. Solids* **4**, 241 (1958).
- [10] Y. Togawa, Y. Kousaka, K. Inoue, and J.-i. Kishine, “Symmetry, structure, and dynamics of monoaxial chiral magnets,” *Journal of the Physical Society of Japan* **85**, 112001 (2016).
- [11] J. Lucassen, M. J. Meijer, O. Kurnosikov, H. J. Swagten, B. Koopmans, R. Lavrijsen, F. Klootwijk, R. Frömler, and R. A. Duine, “Tuning magnetic chirality by dipolar interactions,” *Physical review letters* **123**, 157201 (2019).
- [12] P. Mellado, A. Concha, K. Hofhuis, and I. Tapia, “Intrinsic chiral field as vector potential of the magnetic current in the zig-zag lattice of magnetic dipoles,” *Scientific reports* **13**, 1245 (2023).
- [13] M. Paula and I. Tapia, “Magnetic solitons due to interfacial chiral interactions,” *Journal of Physics: Condensed Matter* **35**, 164002 (2023).
- [14] T. Yu and G. E. Bauer, “Chiral coupling to magnetodipolar radiation,” *Chirality, Magnetism and Magnetoelectricity: Separate Phenomena and Joint Effects in Metamaterial Structures*, 1–23 (2021).
- [15] S. Ray and T. Das, “Hierarchy of multi-order skyrmion phases in twisted magnetic bilayers,” *Physical Review B* **104**, 014410 (2021).
- [16] R. Shindou, J.-i. Ohe, R. Matsumoto, S. Murakami, and E. Saitoh, “Chiral spin-wave edge modes in dipolar magnetic thin films,” *Physical Review B* **87**, 174402 (2013).
- [17] A. P. Malozemoff and J. C. Slonczewski, *Magnetic domain walls in bubble materials: advances in materials and device research*, Vol. 1 (Academic press, 2013).
- [18] A. Hubert and R. Schäfer, *Magnetic domains: the analysis of magnetic microstructures* (Springer Science & Business Media, 2008).
- [19] I. Tapia, X. Cazor, and P. Mellado, “Chiral magnetic phases in moire bilayers of magnetic dipoles,” *Advanced Physics Research* **3**, 2300135 (2024).
- [20] Y. Tokura and N. Nagaosa, “Nonreciprocal responses from non-centrosymmetric quantum materials,” *Nature communications* **9**, 3740 (2018).
- [21] H. Kawamura, “Chirality scenario of the spin-glass ordering,” *Journal of the Physical Society of Japan* **79**, 011007 (2010).
- [22] C. Gong, L. Li, Z. Li, H. Ji, A. Stern, Y. Xia, T. Cao, W. Bao, C. Wang, Y. Wang, *et al.*, “Discovery of intrinsic ferromagnetism in two-dimensional van der waals

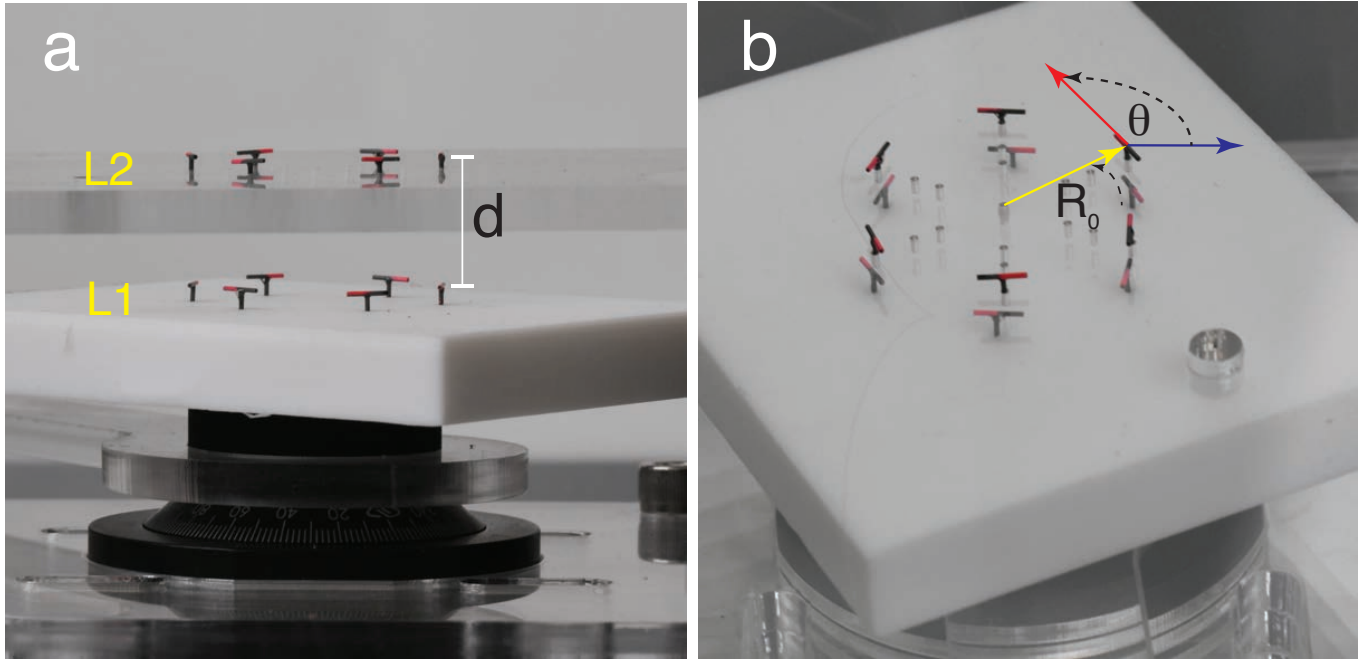


FIG. 1. a.- Bilayer experimental setup: A 10 mm thick Teflon plate (L1) holding 6 Neodymium dipoles can rotate in the XY plane is mounted on a non-magnetic rotational stage. On top and parallel to this layer we set a second layer made out of 5mm cast acrylic that is fixed to a vertical stage that allows fine control of the distance d . Both layers have 4 mm depth holes that allow the graphite axes to freely rotate. b. Top-lateral view of the two layers for small twist ϕ between them. Top and bottom layer hexagons are concentric, and have a side of R_0 . θ is the local rotation angle of a dipole respect to the x-axis (blue arrow).

crystals," Nature **546**, 265–269 (2017).

- [23] G. Chen, T. Ma, A. T. N'Diaye, H. Kwon, C. Won, Y. Wu, and A. K. Schmid, "Tailoring the chirality of magnetic domain walls by interface engineering," Nature communications **4**, 2671 (2013).
- [24] S. Elitzur, R. Pearson, and J. Shigemitsu, "Phase structure of discrete abelian spin and gauge systems," Physical Review D **19**, 3698 (1979).
- [25] G. Sun, T. Vekua, E. Cobanera, and G. Ortiz, "Phase transitions in the z p and u (1) clock models," Physical Review B **100**, 094428 (2019).
- [26] J. V. José, L. P. Kadanoff, S. Kirkpatrick, and D. R. Nelson, "Renormalization, vortices, and symmetry-breaking perturbations in the two-dimensional planar model," Physical Review B **16**, 1217 (1977).
- [27] J. Villain, "Theory of one-and two-dimensional magnets with an easy magnetization plane. ii. the planar, classical, two-dimensional magnet," Journal de Physique **36**, 581–590 (1975).
- [28] J. Cardy, *Scaling and renormalization in statistical physics*, Vol. 5 (Cambridge university press, 1996).
- [29] S. K. Baek, H. Mäkelä, P. Minnhagen, and B. J. Kim, "Residual discrete symmetry of the five-state clock model," Physical review. E, Statistical, nonlinear, and soft matter physics **88**, 012125 (2013).
- [30] Z. Nussinov and J. Van Den Brink, "Compass models: Theory and physical motivations," Reviews of Modern Physics **87**, 1–59 (2015).
- [31] D.-H. Kim, "Partition function zeros of the p-state clock model in the complex temperature plane," Physical Review E **96**, 052130 (2017).
- [32] A. Gopinathan and D. G. Grier, "Statistically locked-in transport through periodic potential landscapes," Physical review letters **92**, 130602 (2004).
- [33] D. J. Amit, Y. Y. Goldschmidt, and S. Grinstein, "Renormalisation group analysis of the phase transition in the 2d coulomb gas, sine-gordon theory and xy-model," Journal of Physics A: Mathematical and General **13**, 585 (1980).
- [34] L. Lemmens, I. Kimura, and W. De Jonge, "Sine-gordon kink solitons and the magnetisation in one-dimensional antiferromagnetic chains," Journal of Physics C: Solid State Physics **19**, 139 (1986).
- [35] A. Concha, D. Aguayo, and P. Mellado, "Designing hysteresis with dipolar chains," Physical Review Letters **120**, 157202 (2018).
- [36] S.-W. Cheong and X. Xu, "Magnetic chirality," npj Quantum Materials **7**, 40 (2022).
- [37] C. D. Batista, S.-Z. Lin, S. Hayami, and Y. Kamiya, "Frustration and chiral orderings in correlated electron systems," Reports on Progress in Physics **79**, 084504 (2016).
- [38] R. Yambe and S. Hayami, "Ferrochiral, antiferrochiral, and ferrichiral skyrmion crystals in an itinerant honeycomb magnet," Physical Review B **107**, 014417 (2023).
- [39] S. Whitsitt, R. Samajdar, and S. Sachdev, "Quantum field theory for the chiral clock transition in one spatial dimension," Physical Review B **98**, 205118 (2018).
- [40] V. Maryasin, M. E. Zhitomirsky, and R. Moessner, "Low-field behavior of an xy pyrochlore antiferromagnet: Emergent clock anisotropies," Physical Review B **93**, 100406 (2016).

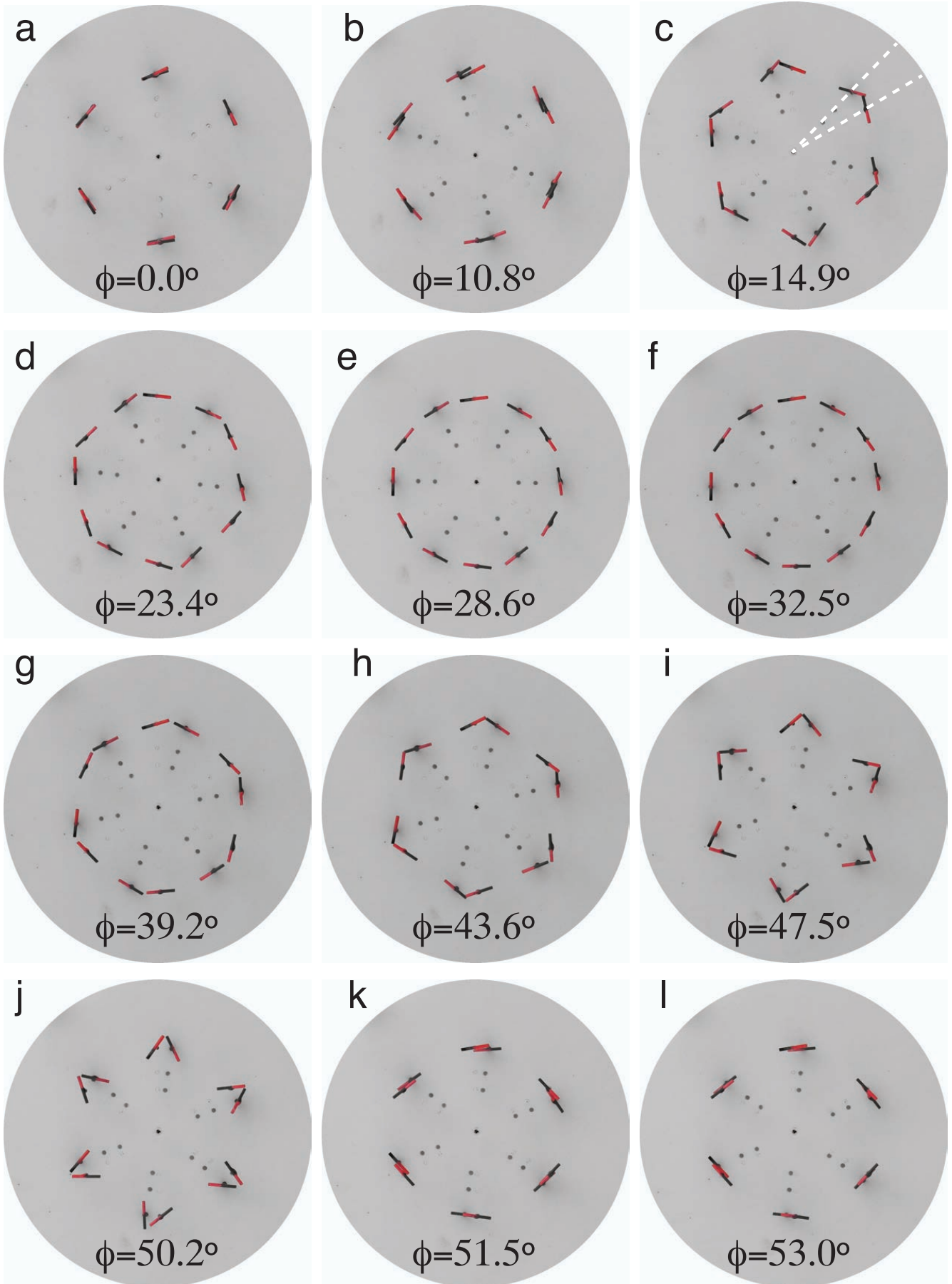


FIG. 2. The evolution of magnetic texture as function of the twisting angle ϕ between the two layers described in Fig.1. Dashed white lines in Fig.2-c show a twisting angle of $\phi = 14.9^\circ$ as an example. The bottom layer rotates and the upper layer (acrylic) stays fixed. The length scale of this panel is defined by the size of each magnet $L = 5\text{mm}$.

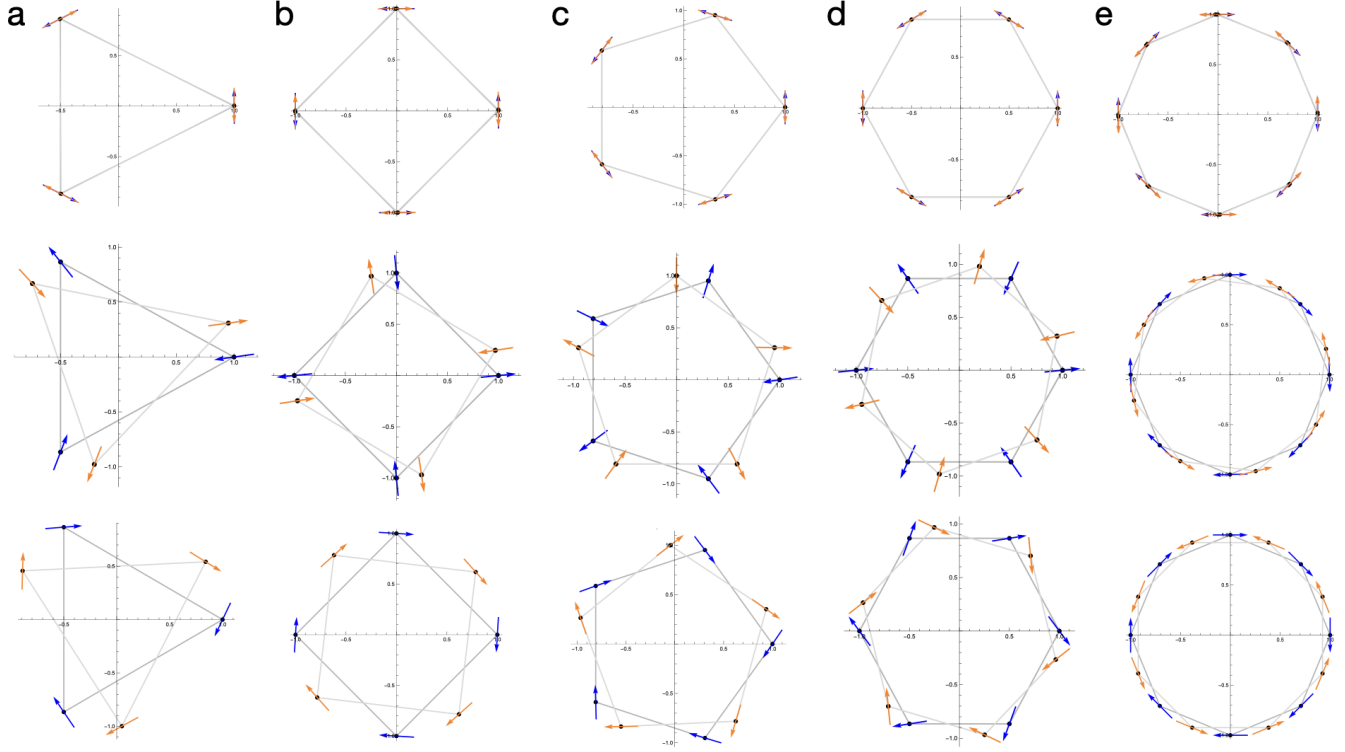


FIG. 3. Equilibrium magnetic configurations of families of bilayers of polygons ($N=3,4,5,6,8$) for three different values of the twisting angle in each case. Results are product of energy minimization of the dipolar Hamiltonian of the systems.

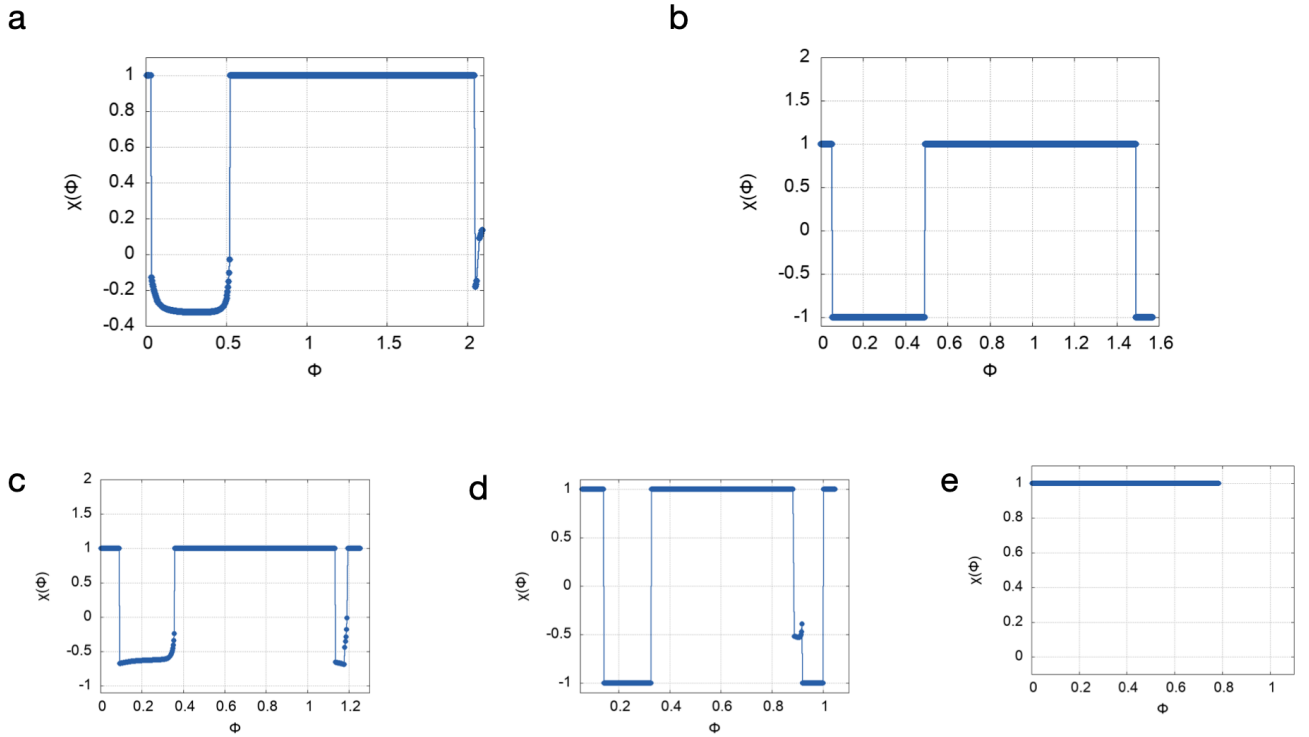


FIG. 4. Chirality order parameter $\chi(\phi)$ in twisted a) triangular, b) squared, c) pentagonal, d) hexagonal, and e) octagonal bipolygons as ϕ was tuned in the range $\phi \in (0, 2\pi/N)$.

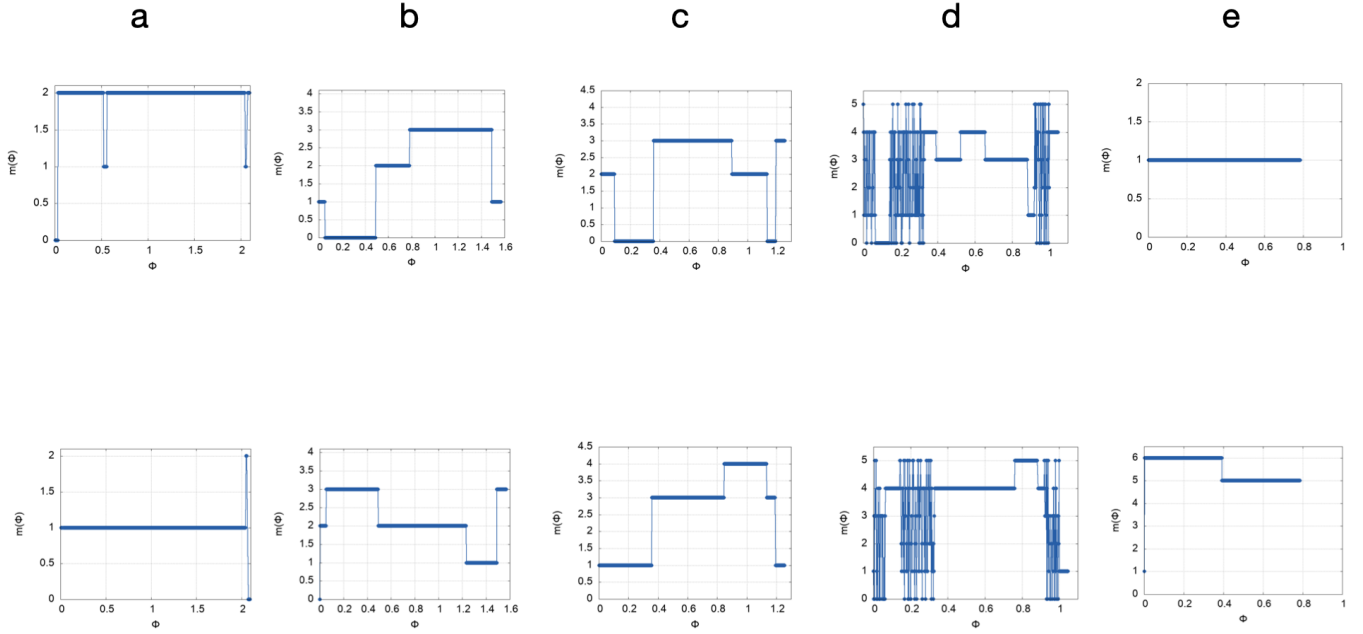


FIG. 5. Clock index $m(\phi)$ in the top and bottom polygon of twisted a) triangular, b) squared, c) pentagonal, d) hexagonal, and e) octagonal bipolygons as ϕ was tuned in the range $\phi \in (0, 2\pi/N)$.

- [41] H. Vignaud, D. Perconte, W. Yang, B. Kousar, E. Wagner, F. Gay, K. Watanabe, T. Taniguchi, H. Courtois, Z. Han, *et al.*, “Evidence for chiral supercurrent in quantum hall josephson junctions,” *Nature* **624**, 545–550 (2023).
- [42] J. Cuevas-Maraver, P. G. Kevrekidis, and F. Williams, “The sine-gordon model and its applications,” *Nonlinear systems and complexity* **10** (2014).
- [43] J. Flaminio and J. Giedt, “Lattice sine-gordon model,” *Physical Review D* **101**, 074503 (2020).
- [44] S. Coppersmith and D. Fisher, “Pinning transition of the discrete sine-gordon equation,” *Physical Review B* **28**, 2566 (1983).
- [45] M. Miller, “Nonlinear wave propagation in periodic systems: The driven sine-gordon chain,” *Physical Review B* **33**, 1641 (1986).
- [46] A. Bruce, R. Cowley, and A. Murray, “The theory of structurally incommensurate systems. ii. commensurate-incommensurate phase transitions,” *Journal of Physics C: Solid State Physics* **11**, 3591 (1978).
- [47] A. M. Popov, I. V. Lebedeva, A. A. Knizhnik, Y. E. Lozovik, and B. V. Potapkin, “Commensurate-incommensurate phase transition in bilayer graphene,” *Physical Review B—Condensed Matter and Materials Physics* **84**, 045404 (2011).
- [48] I. V. Lebedeva and A. M. Popov, “Commensurate-incommensurate phase transition and a network of domain walls in bilayer graphene with a biaxially stretched layer,” *Physical Review B* **99**, 195448 (2019).
- [49] K. Sasaki and L. Floria, “Symmetry-breaking commensurate states in generalised frenkel-kontorova models,” *Journal of Physics: Condensed Matter* **1**, 2179 (1989).
- [50] I. V. Lebedeva and A. M. Popov, “Energetics and structure of domain wall networks in minimally twisted bilayer graphene under strain,” *The Journal of Physical Chemistry C* **124**, 2120–2130 (2019).
- [51] H.-C. Wang and C.-H. Hsu, “Electrically tunable correlated domain wall network in twisted bilayer graphene,” *2D Materials* **11**, 035007 (2024).
- [52] M. A. Kaliteevski, V. Enaldiev, and V. I. Fal’ko, “Twirling and spontaneous symmetry breaking of domain wall networks in lattice-reconstructed heterostructures of two-dimensional materials,” *Nano Letters* **23**, 8875–8880 (2023).
- [53] P. Cazeaux, D. Clark, R. Engelke, P. Kim, and M. Luskin, “Relaxation and domain wall structure of bilayer moiré systems,” *Journal of Elasticity* **154**, 443–466 (2023).
- [54] D. Park, C. Park, K. Yananose, E. Ko, B. Kim, R. Engelke, X. Zhang, K. Davydov, M. Green, H.-M. Kim, *et al.*, “Unconventional domain tessellations in moiré-of-moiré lattices,” *Nature* , 1–8 (2025).